

Co-optimization of linear gain and dynamic range for atomic superheterodyne receivers based on homodyne readout

Chuan Qu(瞿川), Dongqin Guo(郭东琴), and Jian Zhang(张剑)
Citation: Chin. Phys. B, 2026, 35 (**1**): 013202. DOI: 10.1088/1674-1056/ade8e9
http://cpb.iphy.ac.cn; http://iopscience.iop.org/cpb

What follows is a list of articles you may be interested in

Polarization impact on sensitivity of Rydberg atom-based microwave sensors

Minghao Cai(蔡明皓), Aomao Wei(魏奥贸), Shanshan Chen(陈珊珊), and Yuming Huang(黄聿铭)
Chin. Phys. B, 2025, 34 (**8**): 083201. DOI: 10.1088/1674-1056/add005

Optimization strategies for operational parameters of Rydberg atom-based amplitude modulation receiver

Yuhao Wu(吴宇豪), Dongping Xiao(肖冬萍), Huaiqing Zhang(张淮清), and Sheng Yan(阎晟)
Chin. Phys. B, 2025, 34 (**1**): 013201. DOI: 10.1088/1674-1056/ad886a

Microwave field sensor based on cold cesium Rydberg three-photon electromagnetically induced spectroscopy

Yuan-Yuan Wu(吴圆圆), Yun-Hui He(何云辉), Yue-Chun Jiao(焦月春), and Jian-Ming Zhao(赵建明)
Chin. Phys. B, 2024, 33 (**11**): 113201. DOI: 10.1088/1674-1056/ad7579

Electric field intensity measurement by using doublet electromagnetically induced transparency of cold Rb Rydberg atoms

Ting Gong(宫廷), Shuai Shi(师帅), Zhonghua Ji(姬中华), Guqing Guo(郭古青), Xiaocong Sun(孙小聪), Yali Tian(田亚莉), Xuanbing Qiu(邱选兵), Chuanliang Li(李传亮), Yanting Zhao(赵延霆), and Suotang Jia(贾锁堂)
Chin. Phys. B, 2023, 32 (**10**): 103202. DOI: 10.1088/1674-1056/acf120

Atom-based power-frequency electric field measurement using the radio-frequency-modulated Rydberg spectroscopy

Weixin Liu(刘伟新), Linjie Zhang(张临杰), and Tao Wang(汪涛)
Chin. Phys. B, 2023, 32 (**5**): 053203. DOI: 10.1088/1674-1056/aca6db

---

Co-optimization of linear gain and dynamic range for atomic superheterodyne receivers based on homodyne readout

Chuan Qu(瞿川), Dongqin Guo(郭东琴), and Jian Zhang(张剑)†

Information Engineering University, Zhengzhou 450000, *China*

(Received 18 April 2025; revised manuscript received 26 June 2025; accepted manuscript online 27 June 2025)

Rydberg-atom-based superheterodyne receivers integrate self-calibration, high sensitivity, a wide operational frequency range, and phase/frequency resolved detection capabilities, demonstrating broad application prospects as next-generation microwave receivers. Linear gain and linear dynamic range (LDR) are critical metrics for assessing receiver sensitivity and demodulation fidelity, respectively. We numerically solve the four-level master equation and then employ particle swarm optimization (PSO) algorithm to co-optimize linear gain and LDR in atomic superheterodyne receivers based on balanced homodyne detection. Further, we systematically account for dominant dephasing mechanisms in the simulation, encompassing spontaneous decay, transit dephasing, collision dephasing, laser linewidth dephasing, and Doppler averaging. Homodyne readout utilizes both the real and imaginary parts of polarizability for sensing. In the case of the photon shot noise limit, its signal-to-noise ratio (SNR) expression resembles that of direct optical-intensity readout. However, the inherent coherent subtraction operation in homodyne detection significantly suppresses common-mode noise, while appropriately increasing the reference beam power enhances the gain in practical experiments. Indeed, this co-optimization problem, characterized by a high-dimensional variable space, two objectives, and non-convexity, is well-suited for solution by PSO. In addition, probe and coupling detuning contribute equivalently to polarizability and compensate for each other owing to Doppler averaging, thereby reducing the optimization variable space by one. By adopting a product form of linear gain and LDR as the fitness function, the PSO achieves rapid convergence. Here, the effectiveness of the PSO results is verified via the total harmonic distortion (THD). The relative error-based LDR calculation method we proposed efficiently measures receiver response linearity with consuming fewer computational resources. This research is expected to offer valuable insights into enhancing the performance of Rydberg-atom-based superheterodyne receivers.

Keywords: atomic superheterodyne receivers, linear gain, linear dynamic range, balanced homodyne readout

PACS: 32.80.Ee, 42.50.Gy, 84.30.Qi

DOI: 10.1088/1674-1056/ade8e9 **CSTR:** 32038.14.CPB.ade8e9

1. Introduction

Rydberg atom-based receivers have emerged as a transformative platform for microwave electric field sensing, exploiting their large polarizability and microwave-transition dipole moments to enable self-calibration measurements, high sensitivity, and a broad operating frequency band.[1–4] The incorporation of a local oscillator (LO) microwave field into a Rydberg superheterodyne system enables phase-resolved detection and frequency demodulation of microwave signals via atomic coherence mixing.[5,6] Further, the LO field can adjust the energy-level bias of microwave-dressed Rydberg dark states, enabling the system to operate at the optimal gain point for external field signals and thereby significantly enhancing detection sensitivity.[7] Thus, atomic superheterodyne receivers are applied to communication signal demodulation, such as amplitude modulation (AM),[8] frequency modulation (FM),[9] phase shift keying (PSK),[6,10] and quadrature amplitude modulation (QAM),[11,12] as well as microwave spectrometer,[13] microwave polarization vector measurement,[14] and microwave imaging.[15] Optical-readout noise is the primary factor limiting further improvement in system sensitivity.[16] Hence, balanced homodyne detection based on the Mach–Zehnder interferometer (MZI) is introduced to suppress common-mode noise through its inherent coherent subtraction processing.[17,18] Indeed, MZIs are widely employed in quantum sensing and metrology to enable high-precision measurements with shot-noise-limited sensitivity.[19]

In atom-based receiver systems, amplitude modulations of microwave signals are mapped to intensity variations detected by photodetectors. This mapping relationship forms a nonlinear response curve, where the slope corresponds to linear gain. A larger gain implies higher receiver sensitivity. Optical-readout demodulation remains faithful only when the microwave signal amplitude stays within the approximately linear range of the curve, defined as the LDR. When a strong microwave signal exceeds the LDR, it causes significant amplifications in higher harmonic components, which cannot be filtered out in subsequent processing once they are overlapped with valid intermediate frequency signals.[20] Therefore, optimizing multi-variable configurations through theoretical analysis and numerical simulations is of signifi-

†Corresponding author. E-mail: Zhang_xinda.@126.com

© 2026 Chinese Physical Society and IOP Publishing Ltd. All rights, including for text and data mining, AI training, and similar technologies, are reserved.

cance for enhancing detection sensitivity and signal reconstruction fidelity. While previous studies have individually improved upon linear gain and LDR, their co-optimization remains scarcely reported.[20–22] Specifically, the authors in Ref. [23] identified a trade-off between linear gain and LDR in atomic-based receivers. For direct optical-intensity detection, six variables need to be optimized: probe laser detuning and Rabi frequency, coupling laser detuning and Rabi frequency, and LO microwave detuning and Rabi frequency. The high-dimensional variable space, two conflicting objectives, and absence of explicit analytical functions between variables and objectives pose significant challenges. In balanced homodyne detection, both real and imaginary parts of polarizability are exploited for sensing, introducing an additional optimization variable, *i.e.*, the adjustable phase difference between the signal and reference arms of the MZI. This further escalates the complexity and solution difficulty of the optimization problem.

As a swarm intelligence-driven optimization algorithm, PSO is suited for this bi-objective optimization problem involving high-dimensional search spaces, owing to its rapid convergence dynamics, robust global exploration mechanisms, and independence from explicit analytical functions.[24] To better align with practical scenarios, various dephasing processes are incorporated into the simulation framework, including spontaneous decay, transit dephasing, collision dephasing, laser linewidth dephasing, and Doppler averaging. We analyze the roles of individual variables in linear gain, explore the properties of implicit functions, eliminate variables with equivalent contributions, and hence reduce the dimensionality of the variable space. Further, we establish the calculation formulas for linear gain and LDR, and formulate a suitable fitness function for the PSO. Finally, we use THD, a common metric, to validate the effectiveness of the PSO.

2. Atomic superheterodyne receivers based on homodyne readout

The Rydberg atomic superheterodyne receiver with homodyne readout differs from intensity-readout-based counterparts by incorporating an MZI in the transmitted laser path, as schematically illustrated in Fig. 1. The frequency-locked probe and coupling lasers excite the atomic ensemble in the vapor cell at the target wavelengths. As the microwave field propagates through the cell, it modulates the amplitude and phase of the transmitted probe laser, which then interferes with the reference beam at the second beam splitter. The resulting interference patterns are captured by a balanced detector, thereby suppressing intrinsic detector noise and laser intensity fluctuations, both categorized as common-mode noise.[16,17] Additionally, an intensity attenuator in the probe beam path adjusts the probe intensity, while a piezoelectric transducer (PZT) in the reference path modulates the relative phase with the probe beam via changing the path length.

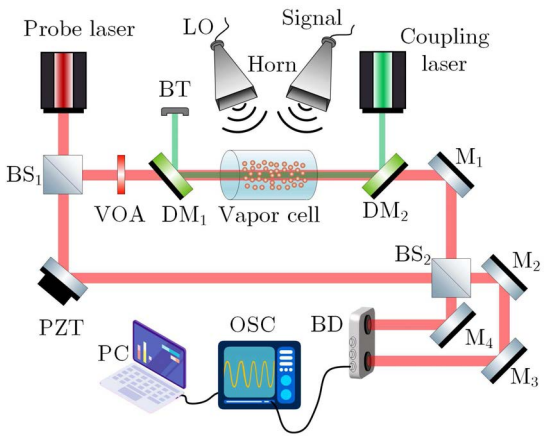


Fig. 1. Schematic diagram of Rydberg atom-based optical balanced homodyne readout for microwave field detection. BS: beam splitter, VOA: variable optical attenuator, DM: dichroic mirror, M: high-reflectivity mirror, BT: beam terminator, PZT: piezoelectric transducer, BD: balanced detector, OSC: oscilloscope, PC: personal computer.

2.1. Master equation and various dephasing mechanisms

We select cesium atoms as the atomic sensor and fill them into an atomic vapor cell. This four-level atomic system comprises a ground state $|1\rangle$: $6S_{1/2}$ ($F=4$), an intermediate state $|2\rangle$: $6P_{3/2}$ ($F'=5$), and two adjacent Rydberg states $|3\rangle$ and $|4\rangle$, $52D_{5/2}$ and $53P_{3/2}$. The transition wavelengths between $|1\rangle \leftrightarrow |2\rangle$ and $|2\rangle \leftrightarrow |3\rangle$ are 852.35 nm and 509.44 nm, respectively. The microwave frequency for the $|3\rangle \leftrightarrow |4\rangle$ transition is 5.044 GHz. In this case, the probe laser drives the $|1\rangle \leftrightarrow |2\rangle$ transition (corresponding to the D2 line), while the coupling laser drives the $|2\rangle \leftrightarrow |3\rangle$ transition. The microwave field is tuned to the $|3\rangle \leftrightarrow |4\rangle$ Rydberg transition. Further, we model the four-level atoms coupled to two light fields and one microwave field using the semiclassical density matrix approach within the master equation framework.[1,2]

$$\frac{\mathrm{d}\rho}{\mathrm{d}t} = -\frac{\mathrm{i}}{\hbar}[H,\rho] + \mathcal{L}, \tag{1}$$

where H denotes the Hamiltonian in the rotating frame with counter-rotating terms neglected, ρ the density matrix, t the time of evolution, and $\mathcal{L}$ the Lindbladian operator accounting for relaxation processes. For the four level system, the Hamiltonian is given by

$$H = \frac{\hbar}{2}\begin{bmatrix} 0 & \Omega_\mathrm{p} & 0 & 0 \\ \Omega_\mathrm{p} & -2\Delta_\mathrm{p} & \Omega_\mathrm{c} & 0 \\ 0 & \Omega_\mathrm{c} & -2(\Delta_\mathrm{p}+\Delta_\mathrm{c}) & \Omega_\mathrm{mw} \\ 0 & 0 & \Omega_\mathrm{mw} & -2(\Delta_\mathrm{p}+\Delta_\mathrm{c}-\Delta_\mathrm{mw}) \end{bmatrix}, \tag{2}$$

where Ω_p, Ω_c, and Ω_mw are the Rabi frequencies for the probe, coupling, and microwave field, respectively. $\Omega_j = \mu_j \mathcal{E}_j/\hbar$, $j = \mathrm{p,c,mw}$, with $\mathcal{E}_j$ and μ_j denoting the respective electric field strengths and dipole moments. Δ_p, Δ_c, and Δ_mw are the

detunings of the probe, coupling, and the microwave field, respectively. Further, the sources of relaxation within the current system are primarily attributed to the spontaneous decay (including blackbody radiation), transit dephasing, collisional dephasing, laser linewidth dephasing and Doppler averaging. As a result, $\mathcal{L}$ can be expressed as

$$\mathcal{L} = \mathcal{L}_{\text{spon}} + \mathcal{L}_{\text{t}} + \mathcal{L}_{\text{col}} + \mathcal{L}_{\text{laser}}. \tag{3}$$

Indeed, considering a specific dephasing mechanism mentioned above, the Lindbladian operator $\mathcal{L}$ can be written as

$$\mathcal{L} = \sum_m \left(\hat{L}_m \rho \hat{L}_m^\dagger - \frac{1}{2}\hat{L}_m^\dagger \hat{L}_m \rho - \frac{1}{2}\rho \hat{L}_m^\dagger \hat{L}_m \right), \tag{4}$$

where $\hat{L}_m = \sqrt{\Gamma_m}|i\rangle\langle j|$, $i, j = 1,2,3,4$, Γ_m is the associated dephasing rate between states $|i\rangle$ and $|j\rangle$. $i \neq j$ corresponds to T1 dephasing (energy relaxation), while $i = j$ corresponds to T2 dephasing (pure dephasing). We calculated the spontaneous decay rates of cesium atomic energy levels using the ARC software package, explicitly accounting for blackbody radiation-induced transitions.[25]

Transit dephasing, a significant dephasing mechanism in thermal vapor sensors, occurs when atoms traverse optical beams. The effective transit dephasing rate Γ_{t} is governed by the mean transit time across the laser beam waist, given by

$$\Gamma_{\text{t}} = \sqrt{\frac{8k_{\text{B}}T}{\pi m_{\text{a}}}} \frac{1}{w_0\sqrt{2\ln(2)}}, \tag{5}$$

where m_{a} is the atomic mass, w_0 is the $1/\text{e}^2$ beam waist, T is the ensemble temperature, and k_{B} is Boltzmann constant.[21] As atoms exit the interaction region, the Rydberg population and inter-state coherence are lost, replaced by newly entering ground-state atoms. Hence, $\mathcal{L}_{\text{t}}$ can be calculated using Eq. (4) with $\hat{L}_m = \sqrt{\Gamma_{\text{t}}}|1\rangle\langle m|$, $m = 1,2,3,4$.

Collisions in the vapor cell constitute a dominant dephasing mechanism. The collision dephasing rate is given by $\Gamma_{\text{col}} = v\rho_{\text{a}}\sigma$, where v is the thermal atomic velocity, ρ_{a} is the density of atoms, and σ is the collision cross section determined by van der Waals and dipole–dipole interactions between Rydberg atoms.[26–28] Here, we use the method described in Ref. [17] to calculate the collision rates. The Rydberg atom density is low, around 0.1% of the ground state, such that Rydberg atom–Rydberg atom interactions are negligible. Rydberg-ground state collisions dominate the relaxation dynamics. Additionally, the intermediate state-ground state collision rates become negligible compared to the spontaneous decay rates for the intermediate states.[27] Further, elastic collisions contribute to T2 dephasing, while inelastic collisions contribute to T1 dephasing. Consequently, the $\hat{L}_m$ operators used to calculate $\mathcal{L}_{\text{col}}$ include $\sqrt{\Gamma_{\text{col}}^{\text{e}}}|3\rangle\langle 3|$, $\sqrt{\Gamma_{\text{col}}^{\text{e}}}|4\rangle\langle 4|$, $\sqrt{\Gamma_{\text{col}}^{\text{i}}}|1\rangle\langle 3|$, and $\sqrt{\Gamma_{\text{col}}^{\text{i}}}|1\rangle\langle 4|$ with $\Gamma_{\text{col}}^{\text{e}}$ and $\Gamma_{\text{col}}^{\text{i}}$ being elastic and inelastic collision rates, respectively.

The Lindbladian term arising from the finite laser linewidths cannot be accurately captured by Eq. (4). Indeed, $\mathcal{L}_{\text{laser}}$ is given by

$$\mathcal{L}_{\text{laser}} = -\begin{bmatrix} 0 & \gamma_{\text{p}}\rho_{12} & \gamma_{13}\rho_{13} & \gamma_{14}\rho_{14} \\ \gamma_{\text{p}}\rho_{21} & 0 & \gamma_{\text{c}}\rho_{23} & \gamma_{24}\rho_{24} \\ \gamma_{31}\rho_{31} & \gamma_{\text{c}}\rho_{32} & 0 & \gamma_{\text{mw}}\rho_{34} \\ \gamma_{41}\rho_{41} & \gamma_{42}\rho_{42} & \gamma_{\text{mw}}\rho_{34} & 0 \end{bmatrix}, \tag{6}$$

where $\gamma_{\text{p,c,mw}}$ are the respective laser linewidths and γ_{mw} is often set to zero.[29,30] $\gamma_{31} = \gamma_{13} = \gamma_{\text{p}} + \gamma_{\text{c}}$, $\gamma_{42} = \gamma_{24} = \gamma_{\text{c}} + \gamma_{\text{mw}}$, and $\gamma_{41} = \gamma_{14} = \gamma_{\text{p}} + \gamma_{\text{c}} + \gamma_{\text{mw}}$. γ_{ij} specifically denotes the laser linewidth-induced dephasing rate between states i, j specifically denotes the laser linewidth-induced dephasing rate between state $|i\rangle$ and state $|j\rangle$, $i, j = 1,2,3,4$. ρ_{ij} stands for the element of the density matrix.

Doppler averaging arises from the Maxwellian velocity distribution of atoms in a thermal vapor cell. The density matrix element ρ_{21} between the ground state and the intermediate state is replaced with its Doppler-averaged counterpart.

$$\widetilde{\rho}_{21} = \frac{1}{\sqrt{\pi}v_{\text{p}}} \int_{-3v_{\text{p}}}^{3v_{\text{p}}} \rho_{21}\left(\Delta_{\text{p}}', \Delta_{\text{c}}'\right) \exp\left(-\frac{v_z^2}{v_{\text{p}}^2}\right) \text{d}v_z, \tag{7}$$

where v_z denotes the atomic velocity component along the laser propagation direction, $v_{\text{p}} = \sqrt{2k_{\text{B}}T/m}$ is the most probable velocity of atoms in thermal motion. The probe and coupling beams counterpropagate. Hence, the probe and coupling detunings are modified with $\Delta_{\text{p}}' = \Delta_{\text{p}} - \frac{2\pi}{\lambda_{\text{p}}}v_z$ and $\Delta_{\text{c}}' = \Delta_{\text{c}} + \frac{2\pi}{\lambda_{\text{c}}}v_z$, where λ_{p} and λ_{c} are the wavelengths of the probe and coupling lasers, respectively.

2.2. Sensitivity

The polarizability of the probe laser is directly proportional to the coherence term ρ_{21}, expressed as

$$\chi = -2\frac{\mathcal{N}\mu_{\text{p}}^2}{\varepsilon_0\hbar\Omega_{\text{p}}}\widetilde{\rho}_{21}, \tag{8}$$

where $\mathcal{N}$ is the total atomic number density and ε_0 is the permittivity of free space.

Further, the power transmittance of the probe beam through the atomic vapor cell can be written as $\mathcal{T} = \exp\left[-2\pi l\text{Im}(\chi)/\lambda_{\text{p}}\right]$, where l is the length of the vapor cell and λ_{p} is the wavelength of the probe laser. The phase shift of probe laser induced by atomic quantum effects can be expressed as $\Delta\varphi = \pi l\text{Re}(\chi)/\lambda_{\text{p}}$. Here, $\Delta\varphi$ represents the phase shift relative to the vacuum by subtracting the vacuum phase shift over the same length. Thus, the transmittance and phase shift are determined by the imaginary and real parts of the polarizability, respectively.

The optical-readout signal of the MZI using balanced detector is given by[16]

$$I_{\text{h}} = 2C\sqrt{P_{\text{s}}P_{\text{r}}}\sin(\Delta\varphi + \phi), \tag{9}$$

where C is the photoelectric conversion coefficient of the detector and the detection efficiency is assumed to be unity. $P_{\rm s}$ and $P_{\rm r}$ denote the laser powers in the signal and reference arms of the MZI, respectively, before recombination at the second beam splitter. ϕ represents the mechanically tunable phase in the reference arm introduced by the PZT. Here, $P_{\rm s} = \mathcal{T}P_{\rm p}$, where $P_{\rm p}$ represents the probe power incident on the atomic vapor cell. The linear gain κ quantifies the sensitivity of the detected signal to $\Omega_{\rm mw}$. In terms of the balanced homodyne detection, it is defined as $\kappa_{\rm h} = \left|\dfrac{\partial I_{\rm h}}{\partial \Omega_{\rm mw}}\right|$. Similarly, the direct detection scheme based on the probe power yields an optical-readout signal $I_{\rm d} = CP_{\rm s}$, with the corresponding linear gain expressed as $\kappa_{\rm d} = \left|\dfrac{\partial I_{\rm d}}{\partial \Omega_{\rm mw}}\right|$.

For Rydberg-atom-based microwave heterodyne receiver, the time-domain expressions for the LO field and the signal field are given by $E_{\rm LO} = \mathcal{E}_{\rm LO}\cos(2\pi f_{\rm LO}t + \phi_{\rm LO})$ and $E_{\rm s} = \mathcal{E}_{\rm s}\cos(2\pi f_{\rm s}t + \phi_{\rm s})$, where $\mathcal{E}_j$, f_j, and ϕ_j (with $j = {\rm LO}, {\rm s}$) denote the respective electric field strengths, frequencies, and phases. Thus, the superposition field $E_{\rm mw}$ resulting from the combination of $E_{\rm LO}$ and $E_{\rm s}$ can be written as

$$\begin{aligned} E_{\rm mw} &= E_{\rm LO} + E_{\rm s} \\ &\approx \mathcal{E}_{\rm LO}\left[1 + \beta\cos(2\pi\Delta f_1 t + \Delta\phi_1)\right]\cos(2\pi f_{\rm LO}t + \phi_{\rm LO}), \end{aligned} \tag{10}$$

where $\beta = \mathcal{E}_{\rm s}/\mathcal{E}_{\rm LO}$, $\Delta f_1 = f_{\rm LO} - f_{\rm s}$, and $\Delta\phi_1 = \phi_{\rm LO} - \phi_{\rm s}$. The atomic sensor's nonlinear response to the superposition field $E_{\rm mw}$ closely approximates envelope detection, with the dominant frequency component being $f_{\rm LO}$.[20] Further, $\Omega_{\rm mw}$ can be written as

$$\Omega_{\rm mw} = \Omega_{\rm LO} + \Omega_{\rm Sig}\cos(2\pi\Delta f_1 t + \Delta\phi_1), \tag{11}$$

where $\Omega_{\rm LO}$ and $\Omega_{\rm Sig}$ denote the Rabi frequencies of the LO and signal fields, respectively. We assume that $\Omega_{\rm Sig}$ equals unity, such that the SNR is given by $\frac{\kappa}{C\eta}$, where η represents the optical readout noise power. Optical readout noise refers to the noise introduced in the process of converting wireless microwave signals into the photodetector's electrical output signals in Rydberg atom-based microwave receivers. This term specifically distinguishes it from the noise present in the incident microwave signals (*i.e.*, background noise) and the noise generated within the backend electrical signal processing system. Indeed, the optical readout noise primarily originates from laser intensity and phase fluctuations, photodetector noise, atomic thermal motion noise, and photon shot noise. For the balanced homodyne detection, $\kappa_{\rm h}$ can be express as

$$\begin{aligned} \kappa_{\rm h} = \Bigg| & C\sqrt{P_{\rm r}P_{\rm p}}\frac{2\pi l}{\lambda_{\rm p}}\sqrt{\mathcal{T}}\big[-{\rm Im}(\chi')\sin(\Delta\varphi+\phi) \\ & + {\rm Re}(\chi')\cos(\Delta\varphi+\phi)\big]\Bigg|, \end{aligned} \tag{12}$$

where χ' denotes the derivative of χ with respect to $\Omega_{\rm mw}$ evaluated at $\Omega_{\rm mw} = \Omega_{\rm LO}$. Similarly, for the intensity-based direct detection, $\kappa_{\rm d}$ is given by

$$\kappa_{\rm d} = \left|CP_{\rm p}\frac{2\pi l}{\lambda_{\rm p}}\mathcal{T}{\rm Im}(\chi')\right|. \tag{13}$$

Therefore, the balanced homodyne detection simultaneously exploits changes in both the real and imaginary parts of the polarizability, whereas the direct detection only utilizes variations in the imaginary part. The coefficient $\sqrt{P_{\rm r}}$ in the expression for $\kappa_{\rm h}$ represents an experimentally tunable parameter that can be increased appropriately, thereby enhancing sensitivity to the signal field. Notably, in practical experiments, increasing the reference beam power may also introduce challenges such as enhanced background light, saturation of optical components, and magnification of imbalance errors in the MZI. Therefore, the reference beam power can be experimentally optimized by balancing signal gain and noise amplification, thereby improving SNR.

Here, we analyze the optical shot noise-limited case. For balanced homodyne detection, the optical shot noise in each detector is uncorrelated, resulting in the subtraction-signal shot noise equaling the sum of the two individual noise contributions, given by $\eta_{\rm h,shot} = \sqrt{(P_{\rm s}+P_{\rm r})\frac{\hbar\omega_{\rm p}}{\tau}}$, where $\omega_{\rm p}$ is the angular frequency of the probe laser, and τ represents the measurement time, which is typically set to 1 s. Therefore, the shot noise-limited SNR for the balanced homodyne detection can be written as

$$\begin{aligned} \frac{\kappa_{\rm h}}{C\eta_{\rm h,shot}} &= \frac{\sqrt{P_{\rm r}P_{\rm p}}\frac{2\pi l}{\lambda_{\rm p}}\sqrt{\mathcal{T}}\left|-{\rm Im}(\chi')\sin(\Delta\varphi+\phi) + {\rm Re}(\chi')\cos(\Delta\varphi+\phi)\right|}{\sqrt{(\mathcal{T}P_{\rm p}+P_{\rm r})\frac{\hbar\omega_{\rm p}}{\tau}}} \\ &\le \sqrt{\frac{\tau}{\hbar\omega_{\rm p}}}\sqrt{P_{\rm p}\mathcal{T}}\frac{2\pi l}{\lambda_{\rm p}}\left|-{\rm Im}(\chi')\sin(\Delta\varphi+\phi) + {\rm Re}(\chi')\cos(\Delta\varphi+\phi)\right| \\ &\le \sqrt{\frac{\tau}{\hbar\omega_{\rm p}}}\sqrt{P_{\rm p}\mathcal{T}}\frac{2\pi l}{\lambda_{\rm p}}\sqrt{\frac{{\rm Im}(\chi')^2 + {\rm Re}(\chi')^2}{2}}, \end{aligned} \tag{14}$$

where the equality condition of the first inequality is satisfied when $P_{\rm r} = \mathcal{T}P_{\rm p}$, while the equality condition of the second inequality holds when $\Delta\varphi + \phi = \frac{\pi}{2} + \arctan\left[{\rm Re}(\chi')/{\rm Im}(\chi')\right] + k\pi$ with $k \in \mathbb{Z}$.

In addition, for the direct detection, the shot noise is given by $\eta_{\mathrm{d,shot}} = \sqrt{P_{\mathrm{s}}\frac{\hbar\omega_{\mathrm{p}}}{\tau}}$. Hence, the the shot noise-limited SNR for the direct detection is given by

$$\frac{\kappa_{\mathrm{d}}}{C\eta_{\mathrm{d,shot}}} = \sqrt{\frac{\tau}{\hbar\omega_{\mathrm{p}}}}\sqrt{P_{\mathrm{p}}\mathcal{T}}\frac{2\pi l}{\lambda_{\mathrm{p}}}\left|\mathrm{Im}(\chi')\right|. \tag{15}$$

Comparison of Eqs. (14) and (15) reveals that the shot noise-limited SNR expressions for balanced homodyne detection and direct detection exhibit analogous forms, with the only distinction lying in the exploitation of the real component of the polarizability by the former. In fact, shot noise is found to be significantly smaller than other components of the optical readout noise.[16] Importantly, the coherent subtraction processing employed in the balanced detection effectively suppresses common-mode noise, and appropriately increasing the reference beam power within the MZI can also boost linear gain, collectively contributing to enhance the SNR.

3. Demodulation principles

As indicated by Eq. (11), the signal field can be directly demodulated from balanced homodyne detection results, with Rydberg atoms serving as mixers. In Eq. (1), we set $\mathrm{d}\rho/\mathrm{d}t = 0$ and hence numerically compute the steady-state solutions of the master equation. The simulations in this work are primarily conducted using the ARC and Rydiqule software packages.[25,31] While continuously sweeping the coupling laser detuning Δ_{c}, we obtain the imaginary and real parts of the polarizability at various microwave field intensities, as shown in Fig. 2. Under microwave field excitation, the imaginary component splits into two peaks with a separation equal to Ω_{mw}. The real part curve remains symmetric about the origin, and its splitting also occurs with increasing external microwave field strength. Notably, when all three external field detunings are zero, the real component of the polarizability becomes identically zero, which is also consistent with the analytical formula derived in Ref. [22].

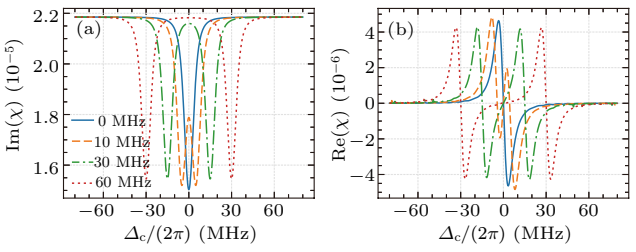


Fig. 2. Numerical results of the polarizability's real and imaginary parts versus Δ_{c} for various microwave field strengths. The values in the legend denote $\Omega_{\mathrm{mw}}/(2\pi)$, with panels (a) and (b) sharing a common legend. The remaining critical parameter configurations are presented as follows: $T = 300$ K, $\Delta_{\mathrm{p}} = \Delta_{\mathrm{mw}} = 0$, $\Omega_{\mathrm{p}}/(2\pi) = 5$ MHz, $\Omega_{\mathrm{c}}/(2\pi) = 1$ MHz, $\gamma_{\mathrm{p}}/(2\pi) = 5$ kHz, $\gamma_{\mathrm{c}}/(2\pi) = 10$ kHz, and $w_0 = 0.75$ mm.

The optical readout signal of the MZI with balanced detection can also be expressed as $I_{\mathrm{h}} = aS$, where a represents a proportionality factor given by $a = C\frac{\hbar}{\mu_{\mathrm{p}}}\sqrt{P_{\mathrm{r}}\pi w_0 c\varepsilon_0/2}$. Here, c denotes the speed of light in a vacuum. The unit of S is Mrad/s, and S can be expressed as

$$S = 2\Omega_{\mathrm{p}}\sqrt{\mathcal{T}}\sin(\Delta\varphi + \phi). \tag{16}$$

In subsequent sections, we replace I_{h} with S and substitute κ_{h} with κ_{s} to denote the linear gain, defined as $\kappa_{\mathrm{s}} = \frac{\partial S}{\partial\Omega_{\mathrm{mw}}} = \frac{\kappa_{\mathrm{h}}}{a}$. For the scenario depicted in Fig. 2, when the coupling light frequency is locked such that $\Delta_{\mathrm{c}}/(2\pi) = 2$ MHz and $\phi = \pi/2$, the received signal S exhibits a nonlinear response to the Rabi frequency of the microwave field, as illustrated by the red curve in Fig. 3. We locate the point Ω_{op} with the steepest slope on this curve, where the linear gain is maximized. Thus, the LO, serving as the static bias point for demodulation, is set to $\Omega_{\mathrm{LO}} = \Omega_{\mathrm{op}}$. According to Eq. (11), within the approximately linear region near Ω_{LO}, variations in the signal field amplitude directly correspond to changes in the received signal S, thus enabling direct demodulation of the baseband signal.

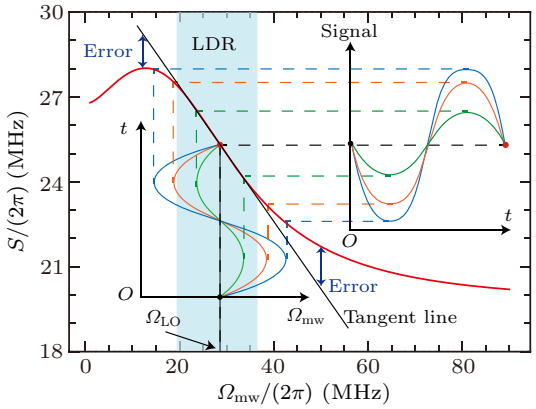


Fig. 3. Schematic illustration of demodulation principle for amplitude-modulated signals in Rydberg atom-based superheterodyne receivers.

As illustrated in Fig. 3, we define the LDR as the interval where microwave field amplitude variations enable high-fidelity demodulation, whereas deviations beyond this operational window induce marked signal distortion. By constructing a tangent line at the Ω_{LO} point on the demodulation response curve, we define the LDR as the interval where the relative error between the demodulation response and the tangent line remains below 1%.

4. Co-optimization of linear gain and LDR employing PSO

Therefore, our research focuses on maximizing both the linear gain κ_{s} and LDR. There are seven variables to optimize: Δ_{p}, Δ_{c}, Δ_{LO}, Ω_{p}, Ω_{c}, Ω_{LO}, and ϕ. Furthermore, considering the Doppler-averaged expression given by Eq. (7), when an additional offset δ is introduced to Δ_{c}, it is shown that

$$\widetilde{\rho}_{21}\left(\Delta_{\mathrm{p}}, \Delta_{\mathrm{c}} + \delta\right) = \frac{1}{\sqrt{\pi}v_{\mathrm{p}}}\int_{-3v_{\mathrm{p}}}^{3v_{\mathrm{p}}}\rho\left(\Delta_{\mathrm{p}} - \frac{2\pi}{\lambda_{\mathrm{p}}}v_z, \Delta_{\mathrm{c}} + \frac{2\pi}{\lambda_{\mathrm{c}}}v_z + \delta\right)\exp\left(\frac{-v_z^2}{v_{\mathrm{p}}^2}\right)\mathrm{d}v_z$$

$$= \frac{1}{\sqrt{\pi}v_{\mathrm{p}}} \int_{-3v_{\mathrm{p}}+\frac{2\pi}{\lambda_{\mathrm{c}}}\delta}^{3v_{\mathrm{p}}+\frac{2\pi}{\lambda_{\mathrm{c}}}\delta} \rho\left(\Delta_{\mathrm{p}} - \frac{2\pi}{\lambda_{\mathrm{p}}}u + \frac{\lambda_{\mathrm{c}}}{\lambda_{\mathrm{p}}}\delta, \Delta_{\mathrm{c}} + \frac{2\pi}{\lambda_{\mathrm{c}}}u\right) \times \exp\left[-\frac{\left(u - \frac{\lambda_{\mathrm{c}}}{2\pi}\delta\right)^2}{v_{\mathrm{p}}^2}\right] \mathrm{d}u$$

$$\approx \widetilde{\rho}_{21}\left(\Delta_{\mathrm{p}} + \frac{\lambda_{\mathrm{c}}}{\lambda_{\mathrm{p}}}\delta, \Delta_{\mathrm{c}}\right), \tag{17}$$

where $u = v_z + \frac{\lambda_{\mathrm{c}}}{2\pi}\delta$ and the third approximation holds when $\frac{\lambda_{\mathrm{c}}}{2\pi}\delta \ll v_{\mathrm{p}}$.

Additionally, we numerically simulated the polarizability as a function of both Δ_{p} and Δ_{c}, as shown in Fig. 4. Here, the dashed lines represent the imaginary (or real) part of polarizability dependence on Δ_{p}, when Δ_{c} is fixed. These curves exhibit the same shape, and as Δ_{c} increases, they shift along the negative Δ_{p}-axis. Thus, under Doppler averaging, Δ_{p} and Δ_{c} contribute equivalently to the polarizability. To reduce experimental complexity, only one laser requires precise frequency tuning.

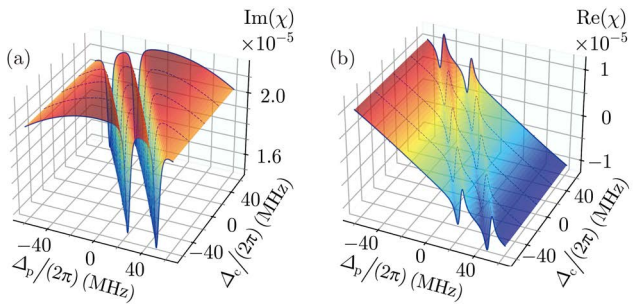


Fig. 4. Numerically simulated polarizability as a function of both Δ_{p} and Δ_{c}. The dashed lines illustrate the polarizabilities varying with Δ_{p} at fixed Δ_{c}. (a) Imaginary component. (b) Real component.

Figure 5 presents the maximal linear gain κ_{s} varying with the Rabi frequencies [Fig. 5(a)] of the probe and coupling lasers and their detunings [Fig. 5(b)], respectively. In Fig. 5(a), the linear gain κ_{s} exhibits multiple extrema, rendering the maximization of κ_{s} a non-convex optimization problem. Additionally, figure 5(b) shows a well-aligned tilted band with a slope of $\lambda_{\mathrm{c}}/\lambda_{\mathrm{p}}$, consistent with Eq. (17). This again indicates that Δ_{p} and Δ_{c} can compensate for each other.

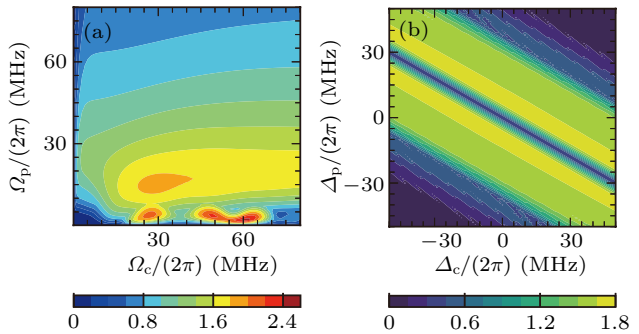


Fig. 5. Numerically simulated contour maps of the maximal linear gain κ_{s} as functions of (a) the Rabi frequencies Ω_{c} and Ω_{p}, and (b) the detunings Δ_{c} and Δ_{p}. In panel (a), $\Delta_{\mathrm{c}}/(2\pi) = 10$ MHz, $\Delta_{\mathrm{p}}/(2\pi) = 0$, $\Delta_{\mathrm{LO}}/(2\pi) = 0$. In panel (b), $\Omega_{\mathrm{c}}/(2\pi) = \Omega_{\mathrm{p}}/(2\pi) = 20$ MHz, $\Delta_{\mathrm{LO}}/(2\pi) = 0$.

Currently, our objective is to optimize the six variables Δ_{c}, Δ_{LO}, Ω_{p}, Ω_{c}, Ω_{LO}, and ϕ to simultaneously maximize both the linear gain and the LDR. Therefore, this problem is modeled as a multivariable, bi-objective, non-convex optimization problem. PSO effectively addresses this challenge through global exploration, adaptive exploitation, and swarm intelligence, without requiring the gradient information. Indeed, the authors in Ref. [23] indicated that linear gain and LDR are two conflicting metrics. Specifically, we define the fitness function in the PSO as their product form, expressed as

$$f = -\kappa_{\mathrm{s}} \ln(R), \tag{18}$$

where R denotes the LDR defined by the relative error mentioned above, expressed in units of Mrad/s. Here, a natural logarithmic transformation is implemented to normalize the scale, thereby establishing numerical equivalence between κ_{s} and $\ln(R)$.

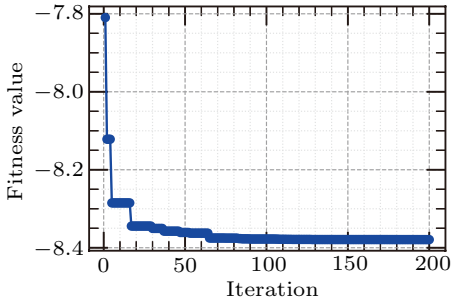


Fig. 6. Fitness convergence curve of the PSO.

We employed 100 particles in the PSO and allowed them to iterate for 200 generations, with the fitness function convergence curve shown in Fig. 6. The fitness function converges rapidly and stabilizes, thereby confirming the effectiveness of the algorithm. In the PSO, the parameter ranges of the six variables and their corresponding optimization results after 200 iterations are presented in Table 1.

Table 1. Optimization variable settings and results.

Optimization variables	Unit	Range	Results
Δ_{c}	MHz	$[-100, 100]$	48.545
Δ_{LO}	MHz	$[-10, 10]$	–6.879
Ω_{p}	MHz	$[0, 150]$	98.744
Ω_{c}	MHz	$[0, 10]$	10.0
Ω_{LO}	MHz	$[0, 150]$	116.500
ϕ	rad	$[0, 2\pi]$	0.963π

Note that the upper bound of Ω_{c} is set to $10 \times 2\pi$ Mrad/s due to the small transition dipole moment of the coupling. When the beam waist diameter of the coupling beam is 1 mm, $\Omega_{\mathrm{c}}/(2\pi) = 10$ MHz corresponds to an optical power of 3.047 W, which already represents a relatively high value in practical experiments. The optimization result of Ω_{c} reaches its upper bound, indicating that increasing Ω_{c} beyond this value may yield better performance. Under the variable configuration provided in Table 1, the variation curves of S and the

corresponding κ_s with Ω_{mw} are shown in Fig. 7(a). The maximum linear gain of $\kappa_s = 1.573$ is achieved when $\Omega_{mw}/(2\pi) = 116.5$ MHz, with an LDR of 32.229 MHz.

In addition, a signal processed by a nonlinear system like the Rydberg atom-based receiver not only retains its fundamental frequency component but also generates various harmonic components, causing the output signal to diverge from the input signal. Thus, THD is employed to measure the degree of signal distortion and is given by

$$D_{TH} = 10\lg\left[\frac{\sum_{n=2}^{\infty}\left(F_n^2 + F_{-n}^2\right)}{F_1^2 + F_{-1}^2}\right], \tag{19}$$

where F_n denotes the n-th harmonic amplitude of the demodulated signal S. Here, n is truncated at the 10th order in the calculation.

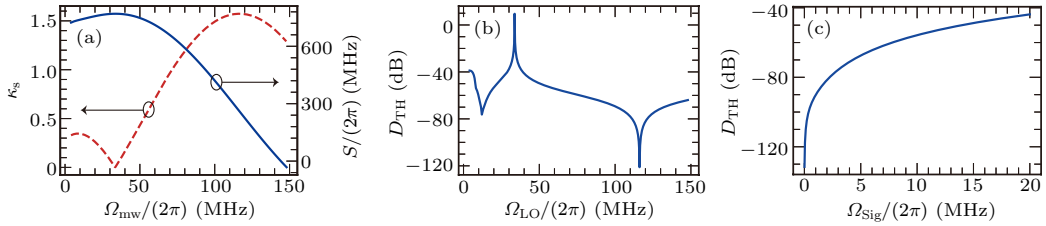


Fig. 7. (a) S and κ_s *versus* Ω_{mw} under the variable configuration obtained by PSO. (b) THD dependence on LO intensity Ω_{LO} for a signal strength of 10 mV/m. (c) THD *versus* Ω_{Sig} with the LO set at the extremum point of the κ_s curve.

Figure 7(b) illustrates the THD variation with Ω_{LO} when $\Omega_{Sig}/(2\pi) = 207.55$ kHz, corresponding to an electric field strength of 10 mV/m. At the extremum of the κ_s versus Ω_{mw} curve, THD reaches its minimum value, indicating that the linear characteristics are optimal at the inflection point of the S curve. Figure 7(c) shows the relationship between THD and the signal strength Ω_{Sig} when the LO set at the S-curve inflection point. When Ω_{Sig} reaches 20 MHz, the THD remains below -40 dB, indicating that the relative error-based LDR calculation method consumes fewer computing resources while effectively evaluating demodulation linearity in parall. In addition, the PSO-obtained LDR is [97.194, 129.424] MHz, and the κ_s extremum does not coincide with the midpoint of the LDR. For large signal amplitudes, adjusting the LO to the LDR midpoint can achieve demodulated signal symmetry.[23]

5. Conclusion

We present a PSO-based co-optimization framework for linear gain and LDR in Rydberg atom superheterodyne receivers with optical balanced homodyne readout. The balanced detection suppresses common-mode noise via coherent subtraction processing, while appropriately increasing the reference beam power in practical experiments also boosts linear gain, synergistically improving the SNR. Owing to Doppler averaging, probe and coupling detunings contribute equivalently to the polarizability and compensate for each other, thereby reducing the optimization variable space by one. Here, the co-optimization of linear gain and LDR constitutes a multivariable, bi-objective, non-convex optimization problem. Given the conflicting nature of these two metrics, their product form $\kappa_s \ln(R)$ is well-suited as the fitness function for the PSO. Further, the PSO converges rapidly, and the obtained results are well validated, achieving a linear gain of 1.573 and an LDR of 32.229 MHz. In addition, the THD characterization also confirms that the relative error-based LDR calculation method we proposed fulfills the requirements for evaluating response linearity, while consuming fewer computing resources.

Acknowledgments

Project supported by the National Natural Science Foundation of China (Grant Nos. 62331024 and 62571549) and the National Key Research and Development Program of China (Grant No. 2022YFB2802804).

References

[1] Sedlacek J A, Schwettmann A, Kübler H, Löw R, Pfau T and Shaffer J P 2012 *Nat. Phys.* **8** 819
[2] Holloway C L, Simons M T, Gordon J A, Dienstfrey A, Anderson D A and Raithel G 2017 *J. Appl. Phys.* **121** 233106
[3] Schlossberger N, Prajapati N, Berweger S, Rotunno A P, Artusio-Glimpse A B, Simons M T, Sheikh A A, Norrgard E B, Eckel S P and Holloway C L 2024 *Nat. Rev. Phys.* **6** 606
[4] Zhang H, Ma Y, Liao K, Yang W, Liu Z, Ding D, Yan H, Li W and Zhang L 2024 *Sci. Bull.* **69** 1515
[5] Meyer D H, Hill J C, Kunz P D and Cox K C 2023 *Phys. Rev. Appl.* **19** 014025
[6] Cai Y, Shi S, Zhou Y, Li Y, Yu J, Li W and Li L 2023 *Phys. Rev. Appl.* **19** 044079
[7] Jing M, Hu Y, Ma J, Zhang H, Zhang L, Xiao L and Jia S 2020 *Nat. Phys.* **16** 911
[8] Li H, Hu J, Bai J, Shi M, Jiao Y, Zhao J and Jia S 2022 *Opt. Express* **30** 13522
[9] Anderson D A, Sapiro R E and Raithel G 2020 *IEEE Trans. Antennas Propag.* **69** 2455
[10] Simons M T, Haddab A H, Gordon J A, Novotny D and Holloway C L 2019 *IEEE Access* **7** 164975
[11] Holloway C L, Simons M T, Gordon J A and Novotny D 2019 *IEEE Antennas Wirel. Propag.* **18** 1853
[12] Nowosielski J, Jastrzębski M, Halavach P, Łukanowski K, Jarzyna M, Mazelanik M, Wasilewski W and Parniak M 2024 *Opt. Express* **32** 30027
[13] Zhang L H, Liu Z K, Liu B, Zhang Z Y, Guo G C, Ding D S and Shi B S 2022 *Phys. Rev. Appl.* **18** 014033
[14] Elgee P K, Cox K C, Hill J C, Kunz P D and Meyer D H 2024 *Phys. Rev. Appl.* **22** 064012

[15] Fan H, Kumar S, Daschner R, Kübler H and Shaffer J 2014 *Opt. Lett.* **39** 3030
[16] Yang W, Jing M, Zhang H, Zhang L, Xiao L and Jia S 2023 *Phys. Rev. Appl.* **19** 064021
[17] Kumar S, Fan H, Kübler H, Sheng J and Shaffer J P 2017 *Sci. Rep.* **7** 42981
[18] Meyer D H, Castillo Z A, Cox K C and Kunz P D 2020 *J. Phys. B: At. Mol. Opt. Phys.* **53** 034001
[19] Cronin A D, Schmiedmayer J and Pritchard D E 2009 *Rev. Mod. Phys.* **81** 1051
[20] Wu F, An Q, Sun Z and Fu Y 2023 *Phys. Rev. A* **107** 043108
[21] Meyer D H, O'Brien C, Fahey D P, Cox K C and Kunz P D 2021 *Phys. Rev. A* **104** 043103
[22] Chen Y, Guo X, Yuen C, Zhao Y, Guan Y L, See C M S, Débbah M and Hanzo L 2025 (*Preprint* arXiv:2501.11842 [cs.IT])
[23] Wu Y, Xiao D, Zhang H and Yan S 2025 *Chin. Phys. B* **34** 013201
[24] Wang D, Tan D and Liu L 2018 *Soft Comput.* **22** 387
[25] Robertson E J, Šibalić N, Potvliege R M and Jones M P 2021 *Comput. Phys. Commun.* **261** 107814
[26] Cao Y, Yang W, Zhang H, Jing M, Li W, Zhang L, Xiao L and Jia S 2022 *J. Opt. Soc. Am. B* **39** 2032
[27] Fan H, Kumar S, Sedlacek J, Kübler H, Karimkashi S and Shaffer J P 2015 *J. Phys. B: At. Mol. Opt. Phys.* **48** 202001
[28] Bai Z, Adams C S, Huang G and Li W 2020 *Phys. Rev. Lett.* **125** 263605
[29] Hanley R K, Bounds A D, Huillery P, Keegan N C, Faoro R, Bridge E M, Weatherill K J and Jones M P 2017 *J. Phys. B: At. Mol. Opt. Phys.* **50** 115002
[30] Bussey L W, Kale Y B, Winter S, Burton F A, Lien Y H, Bongs K and Constantinou C 2024 *EPJ Quantum Technol.* **11** 77
[31] Miller B N, Meyer D H, Virtanen T, O'Brien C M and Cox K C 2024 *Comput. Phys. Commun.* **294** 108952